Composites Science and Technology 174 (2019) 184–193

Contents lists available at ScienceDirect

Composites Science and Technology

journal homepage: www.elsevier.com/locate/compscitech

# Microwave-constructed honeycomb architectures of h-BN/rGO nano-hybrids for efficient microwave conversion

Yue Kang[a,b,*], Wangchang Li[c,**], Tian Ma[b], Xiancong Huang[b], Yaping Mo[d], Zengyong Chu[e], Zhengjun Zhang[a], Guotong Feng[f]

[a] School of Materials Science and Engineering, Tsinghua University, Beijing, 100084, China
[b] Quartermaster Equipment Research Institute, Academy of Military Sciences PLA China, Beijing, 100010, China
[c] College of Materials Science and Engineering, Zhejiang University of Technology, Hangzhou, 310014, China
[d] School of Chinese Language and Literature, Beijing Normal University, Beijing, 100875, China
[e] College of Liberal Arts and Sciences, National University of Defense Technology, Changsha, 410073, China
[f] Qingdao Microwave Creative Technology CO. Ltd, Qingdao, 266000, China

ARTICLE INFO

*Keywords:*
Reduced graphene oxide
BCN
Honeycomb-like structure
Microwave-absorbing property

ABSTRACT

Honeycomb architectures of h-BN/rGO nano-hybrids were built from the self-assemblies of hexagonal boron nitride (h-BN) and graphene oxide (GO) through microwave heating for a few seconds. Incorporation of h-BN nanosheets into 3D reduced graphene oxide (rGO) foams was accompanied by the removal of oxygen-containing groups during the rapid "bread baking" process. TEM and SEM images revealed the layer-stacked structure of the samples. XPS, Raman and XRD spectra showed the presence of h-BN layers that were interlaced into the honeycomb architectures of rGO frameworks. The microwave absorption properties and the complex permittivity could be adjusted by varying the microstructure and the content of h-BN. For the wax composite filled with 6.25 wt% h-BN/rGO nano-hybrid with thickness of 1.8 mm, the reflection loss value reached −35.63 dB at 17.2 GHz, and the effective frequency bandwidth reached 6.96 GHz at 2.6 mm with a low surface density. The honeycomb architecture of the hybrid provided multiple electromagnetic transmission paths and consumed significant amount of microwave energy due to the multiple interfaces. Embedding h-BN in the architecture enables excellent impedance matching, and provides highly efficient dielectric material that can be used for microwave absorption. This work demonstrates that microwave treatment is a facile approach to obtaining optimal microwave absorbing properties of h-BN/rGO nano-hybrids.

## 1. Introduction

Electromagnetic interferences are becoming more and more severe due to the extensive utilization of electronic devices in daily life [1–3]. One of the simple methods to attenuate interfering electromagnetic energy is the use of microwave absorbing materials. The microwave absorption property is not only related to the intrinsic properties of the materials, but also influenced by the macro-/micro-structures of the materials [4,5]. Usually, lightweight, wide absorption, thin thickness and strong absorption are the ideal requirements of advanced microwave absorbers, either for modern stealth weapons or future electronic devices [6–10]. Common microwave absorption composites are fabricated from magnetic or dielectric fillers and various matrices [11–15]. However, their drawbacks such as high density, narrow absorption band, and low mechanical performance, have severely hindered their practical applications. New materials and new concepts are constantly required in this field in order to achieve excellent electromagnetic absorbing performance.

The carbon nanostructures is considered as a valid way to attain lightweight composites and have been receiving increasing attention, such as carbon nanotubes (one-dimensional structure, 1D) [16], graphene (two-dimensional structure, 2D) [17], and carbon foams (three-dimensional structure, 3D) [18]. Although graphene is a candidate material for electromagnetic wave absorption with large surface area, the permittivity of pristine graphene is too high for impedance matching, thus giving rise to intense reflections at the surface [19]. Compared with the 2D layered structures, 3D porous reduced graphene oxide foams (rGOFs) not only exhibit much lower bulk density, but also

* Corresponding author. School of Materials Science and Engineering, Tsinghua University, Beijing, 100084, China.
** Corresponding author.
*E-mail addresses:* goodluckky@163.com (Y. Kang), wcli@zjut.edu.cn (W. Li).

https://doi.org/10.1016/j.compscitech.2019.02.029
Received 9 November 2018; Received in revised form 19 February 2019; Accepted 25 February 2019
Available online 01 March 2019

present thousands of transmitting channels and reflecting interfaces [18,20]. Microwaves can easily enter the architectures and convert to heat in the long transmitting pathways. rGOFs have much smaller effective permittivity than pure graphene, which is helpful for impedance matching [18]. In order to enhance the absorption efficiency and to widen the effective absorption bandwidth of graphene based-nanosheets, atomic doping or layer stacking has been attempted [20,21]. Substituting C atoms with N and B atoms can result in n- and p-type graphene [22]. B and N co-doped graphene may form B−C−N phases with tunable band gaps [23]. Furthermore, h-BN and graphene can be used to form a layer-stacked structure, which could possibly enhance the attenuation of electromagnetic waves [24]. B/N doped graphene has been prepared using hydrothermal, thermal annealing or chemical vapor deposition (CVD) methods [25,26]. However, these approaches are generally time-consuming. It is essential to develop a feasible, effective and environment friendly approach that surpasses the conventional strategies.

Since the 1980s, microwave equipment has progressively entered chemical laboratories and is now being widely used to fabricate a variety of nanostructures with different compositions [27]. Microwave heating, based on the interaction of matter with electromagnetic radiation, is characterized by fast heating rate, low-cost and scalable production. Therefore, it is well-suited as the heating source for carbon reduction method. Microwave irradiation promotes the rapid reduction process of GO into the highly conductive rGO, with the microwave energy transformed into heat. Graphene is regarded as an excellent microwave absorbent while GO has poor microwave absorption capacity. The unoxidized graphitic region 'impurities' in GO act as microwave absorbents, leading to avalanche-like deoxygenation reaction of GO and formation of graphene under microwave irradiation [28,29]. Recently, Kim and co-workers [30] reported a reduced B/N co-doped graphene hybrid via an efficient two-step microwave-hydrothermal synthesis, which involved simultaneous doping with different heteroatoms (B and N) and decrease in doped graphene oxide. However, the preparation method was not simple.

Herein, the one-step rapid synthesis of h-BN/rGO nano-hybrids with honeycomb architectures using a "bread baking" microwave process is reported. GO and h-BN were used as the raw materials. The microwave absorbing properties of the hybrids were determined by the h-BN content. It is noteworthy that layer-stacked h-BN/GO hybrids rapidly reduced and expanded to honeycomb architectures under microwave treatment within a few seconds, as soon as 25 s. The h-BN/rGO nano-hybrids exhibit the excellent electromagnetic wave absorption properties in terms of both the absorption intensity and bandwidth. It is believed that such nano-hybrids absorber will find its wide application in the electromagnetic wave absorption field.

## 2. Experimental section

### 2.1. Raw materials

rGO and h-BN/rGO nano-hybrids were synthesized from h-BN and GO, which were used as nitrogen, boron and carbon sources. h-BN nanosheets were exfoliated as reported (Fig. S1, Supporting Information) [31]. Graphene oxide (GO) was purchased from XFNANO Co. Ltd. Nevertheless, all chemicals used were not further purified.

### 2.2. Synthesis

The detailed synthesis method is described as follows: Precursor solution was prepared by combining graphene oxide and hexagonal structure BN in ethanol, followed by stirring until they were fully dissolved. The mixture was then dried at 60 °C for 6 h in an electric vacuum drying oven. Then, the dried mixture was placed in a commercial microwave oven (Qingdao Microwave Creative Technology Co. Ltd, MW-R10L), where it was heated with an oven output of 4000 W for 25 s to obtain the honeycomb architectures of h-BN/rGO nano-hybrids. A bright light was observed during the reduction process due to the electric arc.

### 2.3. Characterization

The morphologies of the rGO and h-BN/rGO nano-hybrids nanostructures were featured by transmission electron microscopy (TEM, JEM-2100F), scanning electron microscope (SEM, JSM-6700F microscope) and atomic force microscope (AFM). The crystalline structure was examined by X-ray diffraction (XRD) using Bruker D8 X-ray diffractometer with Cu Ka radiation from 5° to 90°(2θ). The fourier transform infrared (FT-IR) spectra were conducted (Nicolet magna-IR 760 spectrometer) in air by using the KBr pellet method. The Ultraviolet–visible (UV–Vis) spectroscopy was logged at indoor temperature with a UV-1800 spectrophotometer. X-ray photoelectron spectroscopy (XPS) was functioned using K Alpha 1063 type spectrometer for measured the existence of functional groups and the changes in the atomic ratios. Energy dispersive X-ray spectroscopy (EDS) analysis was conducted using the related equipment of SEM. To research the defect structures, Raman spectra, with a 514 nm laser excitation, were taken on a LABRAM-010 Raman spectrometer. At indoor temperature, the powder resistance was measured using ST-2722 type powder resistance tester by a four-point probe method. Brunauer Emmett Teller (BET) surface areas were got form a nitrogen adsorption desorption isotherm at 77 K. As mentioned in the previous work [24], the electromagnetic parameters of the h-BN/rGO nano-hybrids were measured by an Agilent 8720 ET vector network analyzer at 2–18 GHz, and the paraffin wax (93.75 wt%) and hybrids (6.25 wt%) were pressed into a cylinder shape (Φout, 7.0 mm; Φin, 3.0 mm). RL (dB), as the reflection loss, was calculated with the electromagnetic parameters using our-self programmed software.

## 3. Results and discussion

### 3.1. Microstructure and composition

Fig. 1 schematically illustrates the experimental process of

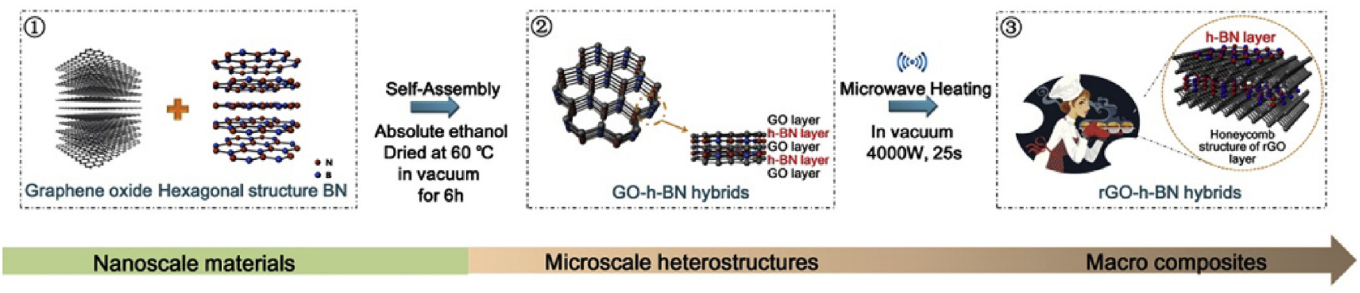


**Fig. 1.** Schematic of the simple route to synthesize h-BN/rGO nano-hybrids.

**Table 1**
Typical hybrids and their processing parameters.

| Sample | GO (wt %) | h-BN (wt %) |
|---|---|---|
| rGO | 100 | |
| BCN20 | 80 | 20 |
| BCN25 | 75 | 25 |
| BCN50 | 50 | 50 |
| BCN75 | 25 | 75 |
| BCN80 | 20 | 80 |

synthesizing h-BN/rGO nano-hybrids. Few-layer and large GO nanosheets, as analyzed, were made ready by a modified Hummers method (Fig. S2) [23,24]. The obtained GO was thoroughly mixed with a solution of h-BN in ethanol with the aid of ultra-sonication. The interaction between h-BN and single-layer GO facilitated the self-assembly of the hybrids. After ultrasonic treatment, the mixture was heated to obtain a thick viscous liquid, and then the hybrids were dried at the same temperature. The dried mixture was placed in a commercial single-functional microwave oven and subjected to microwave heating under vacuum to obtain the h-BN/rGO nano-hybrids, namely the "baking bread" process.

By altering the mass ratios of the raw materials, a series of h-BN/rGO nano-hybrids could be obtained, as listed in Table 1. For instance, the sample label BCN20 indicates that the mass fraction of h-BN was 20 wt% in the raw materials. Other products were accordingly labelled as BCN80, BCN75, BCN50, and BCN25.

Illuminated by the works mentioned above, it is expected that GO with a high defect density and many oxygen-containing functional groups would be more reactive than graphene (or reduced GO). Most importantly, even after the harsh oxidation treatment of Hummer method, it was found that GO still contained some $sp^2$-bonded regions. These graphitic region 'impurities' may actually act as the initiators of the deoxygenation reaction. Microwaves were efficiently dissipated via electrons moving through it, resulting in the super-heating of graphene, which contributed to the local deoxygenation reaction of GO adjacent to graphene. Then, the layer-stacked GO-h-BN rapidly expanded in shape and volume and was successfully embedded with h-BN nanosheets during the rapid partial reduction of "baking bread" process in response to a change in temperature. Therefore, preparing h-BN layers with 3D graphene foams using microwave heating method can be considered as a feasible route for the synthesis of efficient electromagnetic wave attenuating materials on a large-scale.

Common heating methods, such as tube furnace heating, hydrothermal methods, etc., allow the transfer of heat "from the outside to the inside", meaning from the surface of the sample to the interior of the sample. This process is similar to "baking cookies". One side of the "cookies" is heated, and the heat flows from the pan due to the inhomogeneous heat. However, the electromagnetic radiation enables the substitution/doping in a matter of seconds. Similar to the process of "baking bread", polar molecules (or graphitic region 'impurities') pull, push, and collide with other molecules (through electrical forces), which disperses the energy to adjoining molecules and atoms in the material under the alternating field. Moreover, oxygen-containing functional groups were eliminated during the "baking bread" process and the honeycomb-like h-BN/rGO structure, as the "porous bread", was rapidly formed in the total material. In such layered 3D-structured materials, it is expected that the large number of interfaces would increase the electromagnetic transmission path and that a considerable amount of electromagnetic energy would be consumed by the multiple interfaces.

Fig. 2(a-d) and Fig. S3 show the typical SEM images of rGO and h-BN/rGO nano-hybrids. All the samples showed a honeycomb and sandwich-like structure in the micrometer-scale. Among these samples, the skeletons of ultrathin GO nanosheets were smooth, well-stacked and interconnected (Figs. S2(a–b)). After microwave treatment, the cross-section of rGO showed a honeycomb-like structure, which is beneficial to the microwave absorption (Fig. 2(b–d)). From Fig. 2(c-d) and Figs. S3(c–h), it can be seen that after reacting with h-BN nanosheets, the h-BN/rGO nano-hybrids maintained the 3D honeycomb-like structure, implying that the basic structure of hybrids was not damaged during the reaction. At the same time, the layered h-BN was stacked between the honeycomb-like rGO in different states, throughout the entire area. Fig. 2(e-f) and Figs. S2(a–b) show the typical TEM images for the BCN50 hybrid prepared by the reaction of h-BN with GO nanosheets, resulting in wrinkles and folds. It indicates the presence of few-layered graphene in hybrids, which is covered with the h-BN nanosheets. The SAED pattern, as shown in the inset image of Fig. 2(e), further confirmed the unique hexagonal structure of BN and graphene [32]. Besides, the thickness of BCN50 hybrids was analyzed by AFM, as shown in Fig. 2(g) and Fig. S2(c). It indicates that the BCN nanosheets still retained their layered structure, with thickness close to 1.15 nm. In addition, the layer size of the h-BN/rGO nanosheets ranged from 2 to 10 μm.

Fig. 3 illustrates the EDS mapping results of the BCN50 nanosheets. The lateral distributions for B, N, C, and O atoms in the nanosheets, as exhibited in Fig. 3(b–e), indicated that h-BN nanosheets were present in the same regions with relatively few rGO layers. It confirmed the presence and the layered distribution of B, C, N, and O elements, which indicates the intercalated structure of the h-BN/rGO nano-hybrids.

Fig. 4(a) and Fig. S4(c) display the typical Raman spectra of rGO and h-BN/rGO nano-hybrids. The peaks centered at ~1585 and ~1340 $cm^{-1}$ corresponded to G and D bands for all samples [33]. G band and D band are usually related to the in-plane bond extension of $sp^2$ C pairs and the defects or lattice distortion, respectively [34,35]. In this study, both D and G bands were stretched in h-BN/rGO nano-hybrids compared to rGO. It suggests that the defects and lattice distortion increased as the h-BN nanosheets were incorporated.

The intensity ratio of D band and G band, $I_D/I_G$, is directly associated with the average defect distance, $L_a$, and defect density [35–37]. It is usually quantified using the Tuinstria-Koening relation:

$$I_D/I_G = C(\lambda)/L_a \quad (1)$$

The proportionality constant C(λ) depends on the excitation laser wavelength λ. This equation was first used to obtain the size of crystalline $sp^2$ clusters ($L_a$). Furthermore, it has been widely applied to calculate the density of defects in $sp^2$ carbons, including electron induced defects in rGO and h-BN/rGO nano-hybrids (Table 2). Generally, higher value of $I_D/I_G$ indicates more B and N dopants in rGO. The $I_D/I_G$ value of BCN80 was lower than that of the other samples, which indicates that the higher content of h-BN hindered the reaction process, resulting in π-π stacking and a decrease in the defect distance. For the other samples, the $I_D/I_G$ value increased from 1.02 (rGO) to 1.58 (BCN75), revealing that embedding more h-BN in the architecture established more defects and lattice distortion in the h-BN/rGO networks.

In general, high $I_D/I_G$ values indicate high disorder in carbon materials or considerable defects [38]. The above results suggest that the incorporation of h-BN nanostructures could separate the honeycomb-like rGO structure, enhance the grain boundaries between h-BN and rGO and decrease the surface area of h-BN/rGO nanosheets. As shown in Table 2, the change in surface area was significant in the case of rGO (279.276 $m^2/g$) compared to BCN80 (4.425 $m^2/g$). The larger specific surface area of h-BN/rGO nano-hybrids would lead to more defects on their surface. Hence, the disorder or defects inside materials could perform like a 'micro-capacitor' and improve dielectric permittivity, which is usually referred to as space charge polarization. This phenomenon would significantly increase the microwave consumption.

Fig. 4(b) and Fig. S4(b) present the Fourier transform infrared (FT-IR) spectra acquired from rGO and h-BN/rGO nano-hybrids. The FT-IR spectrum of rGO showed strong, broad peaks at ~1051, ~1273 and ~1541 $cm^{-1}$, indicating the presence of alkoxy C—OH group stretching vibrations, in-plane O—H stretching vibrations and aromatic C═C and

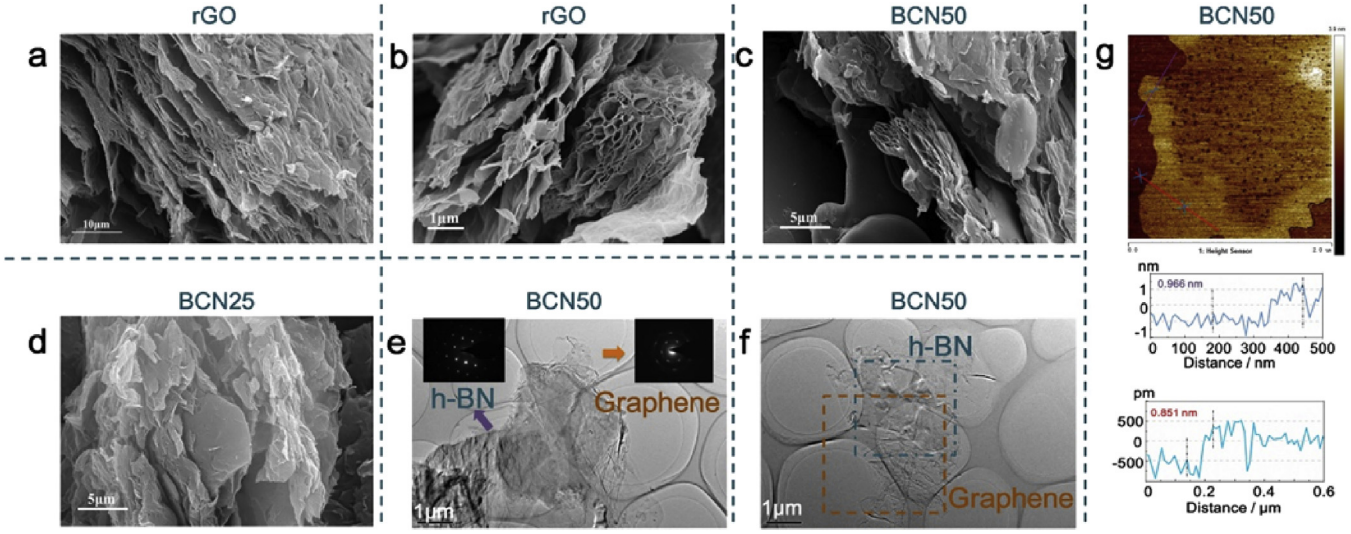


**Fig. 2.** Typical SEM images of (a–b) Reduced graphene oxide; (c) BCN50 hybrid; (d) BCN25 hybrid; Typical TEM images of BCN50 hybrid. (e–f) low-magnification images, indicating h-BN layer combined with the rGO lattice. The inset in (e) is the corresponding SAED of the h-BN and rGO regions. (g) AFM images and corresponding height profiles of BCN50 hybrid.

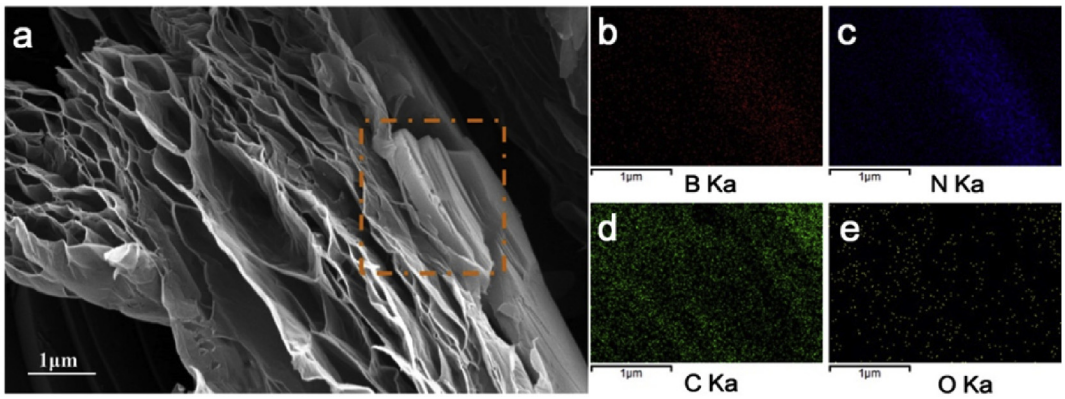


**Fig. 3.** SEM images and corresponding EDS elemental maps for B, C, O and N elements of h-BN/rGO nano-hybrids.

C═O stretching, respectively [39]. The as-prepared h-BN/rGO nano-hybrids exhibited new peaks. The peaks at ~1374 and ~818 $cm^{-1}$, and ~1109 $cm^{-1}$, corresponded to in-plane B—N vibration and $sp^3$ hybrid B—C vibration [40,41]. This result indicated that h-BN nanosheets were embedded in rGO, consistent with the XPS results. In addition, the XRD spectra confirmed the presence of different structures of honeycomb-like graphene [20] and h-BN nanosheets [22] (Fig. S4(a)). Furthermore, the *d*-spacing of nano-carbon layers in rGO and h-BN/rGO nano-hybrids was ~0.89 nm (GO), which decreased to ~0.38 nm (rGO). This change can be ascribed to the removal of oxygen-containing functional groups, as confirmed by FTIR and XPS data.

Fig. 4(c-i) and Fig. S5 show the XPS results for elemental B, C, N, and O measured from rGO, BCN50, and BCN25. The full spectra of rGO, BCN25, and BCN50 in Fig. S5(a) confirmed the existence of B, C, N and O elements [42,43].

The C1s peak of rGO shown in Fig. 4(i) can be deconvoluted into three peaks centered at 284.6, 286.1 and 288.38 eV, which were attributed to C—C bonds, C—OH bonds and C-R bonds originally present in GO nanosheets. Compared to GO (shown in Figs. S5(e–f)), the decreased intensity of C—OH and C-R peaks of rGO suggested that microwave treatment eliminated the oxygen-containing functionalities and $sp^3$ carbons [42]. The B1s signal of BCN50 hybrid is shown in Fig. 4(f). The one main band at 190.48 eV was assigned to C—B—N bond. The C1s peak of BCN50 hybrid is shown in Fig. 4(g), which can be deconvoluted into four peaks, centered at 284.56 eV (C—C bonds), 286.1 eV (C—N bonds), 287.9 eV (C—O bonds) and 288.38 eV (C-R bonds), respectively. The intensity of C—O bonding in the BCN50 hybrid was much weaker than that in GO, revealing the elimination of the oxygen functionalities after microwave treatment and the incorporation of B and N. The N1s peaks in Fig. 4(h) appeared at 398.8 eV (B—N—C bonds) and 398.1 eV (N—B bonds). Based on the intensity and energy of the major peaks in B1s and N1s spectra, it was inferred that the main configuration for B and N atoms was the B—N bond, revealing the presence of B—C—N domains in hybrids.

The B1s peaks for B—O and B—N bonds of BCN25 hybrid were widened compared to those of BCN50 hybrid, indicating that higher content of GO led to better reaction and to the simultaneous embedding of h-BN nanosheets in rGO layers. In short, the XPS results demonstrated that h-BN nanosheets were successfully embedded in the architecture of the hybrids and the unnecessary oxygen-containing groups in the carbon lattice of GO were removed.

The atomic ratios of B, C, N and O in the various samples are shown in Table 3. The chemical formulas for BCN50 and BCN25 are $B_{1.0}C_{2.1}N_{0.8}O_{0.3}$ and $B_{1.0}C_{7.5}N_{0.7}O_{0.9}$, respectively.

### 3.2. Complex permittivity

The real part ($\varepsilon'$) and the imaginary part ($\varepsilon''$) of complex permittivity ($\varepsilon_r = \varepsilon' - j\varepsilon''$) were determined because they indicate the amount

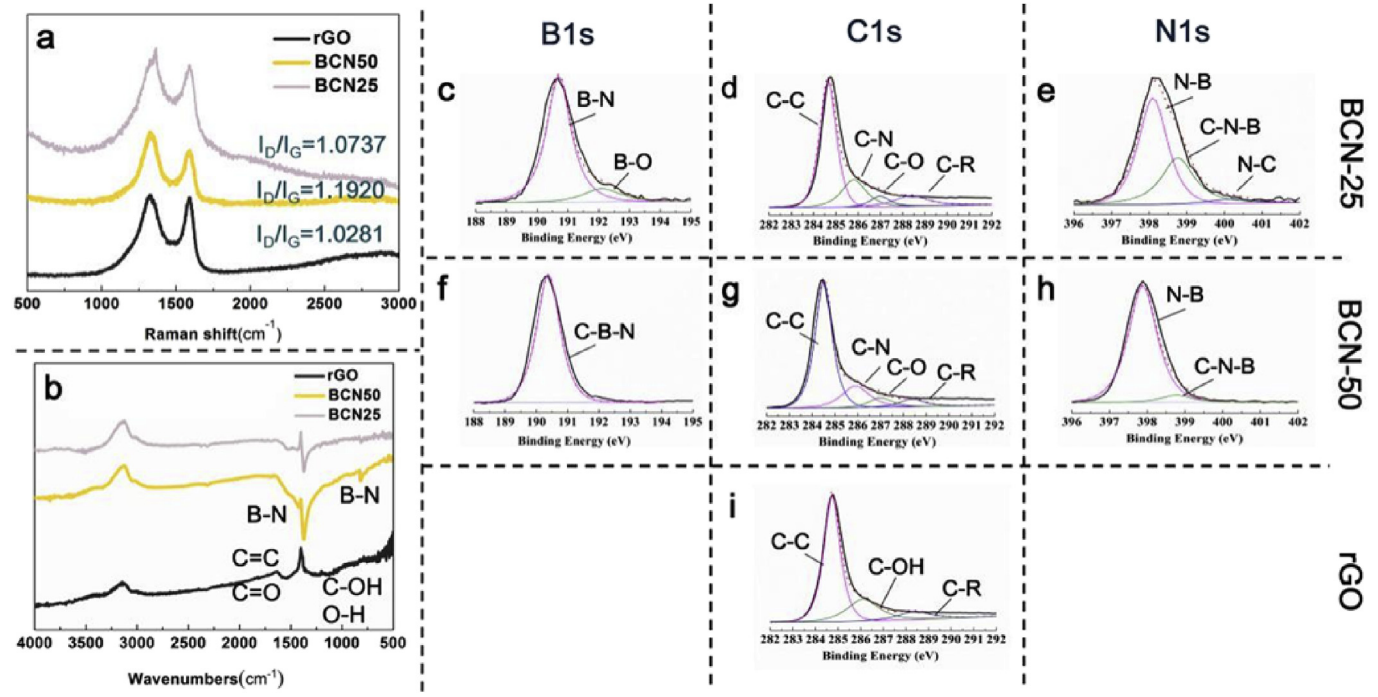


**Fig. 4.** (a) Raman spectra of rGO, BCN50 and BCN25 hybrids. (b) FT-IR spectra of rGO, BCN50 and BCN25 hybrids. (c–i) XPS spectra of rGO, BCN50, and BCN25 hybrids. (c–e) deconvoluted curves of BCN25; (f–h) deconvoluted curves of BCN50; (i) deconvoluted curves of rGO shown in solid lines. The curves were deconvoluted by Gaussian fitting, thereby indicating possible bonding structures.

**Table 2**
$I_D/I_G$, $L_a$ and BET parameters of rGO and h-BN/rGO nano-hybrids.

| | rGO | BCN-20 | BCN-25 | BCN-50 | BCN-75 | BCN-80 |
|---|---|---|---|---|---|---|
| ID/IG | 1.0280 | 1.0617 | 1.0737 | 1.1920 | 1.5856 | 0.9778 |
| La (nm) | 4.28 | 4.14 | 4.09 | 3.69 | 2.77 | 4.49 |
| Specific Surface Area ($m^2/g$) | 279.276 | 182.100 | 87.389 | 62.168 | 4.669 | 4.425 |

**Table 3**
Atomic content and atomic ratios of the hybrids.

| Element | rGO | | BCN25 | | BCN50 | |
|---|---|---|---|---|---|---|
| | atom % | ratio | atom % | ratio | atom % | ratio |
| B | | | 9.73 | 1.0 | 23.22 | 1.0 |
| C | 94.41 | | 73.66 | 7.5 | 49.64 | 2.1 |
| N | | | 7.48 | 0.7 | 19.83 | 0.8 |
| O | 5.59 | | 9.14 | 0.9 | 7.31 | 0.3 |

of polarization occurring in the materials, and represent electromagnetic energy storage and dissipation, respectively [44].

Fig. 5(a-b) shows the real part (ε′) and the imaginary part (ε′′) of complex permittivity in the frequency range from 2 to 18 GHz. Both ε′ and ε′′ values decreased gradually with slight fluctuations, which was attributed to dielectric relaxation. A very high value of permittivity may lead to severe reflection and weak absorption, which would be unfavorable for impedance matching. Thus, a low real part of permittivity and a suitably high imaginary part of permittivity would be ideal for microwave absorbing materials. As shown in Fig. 5(a and b), the ε′ and ε′′ values of rGO were larger than those of BCN hybrids with different h-BN filler contents. This result indicated that the polarization efficiency and energy dissipation of rGO were stronger than those of the other BCN hybrids due to the partly free electrons in the π-π conjugate bond in the plane of graphene oxide. The elimination of oxygen-containing functional groups in GO can enlarge the interlayer distance of rGO. This enhanced inter-layer space would be beneficial to adjust the conductive network as polarization interface. The conductive network formed by honeycomb-like structure of rGO can act as the electronic transmission carrier, thus improving the dielectric loss of the absorber and consuming the electromagnetic energy.

GO itself is a kind of insulator with infinite resistance while graphene is a good conductor [35]. As listed in Table 4, the honeycomb-like structure rGO had a powder resistance of $66.6 \times 10^{-3}$ Ω. As a good insulator, the incorporation of h-BN in graphene will impact the electrical conductivities. When h-BN was incorporated, the powder resistance was improved to $83.9 \times 10^{-3}$ and 0.68 Ω for BCN25 and BCN50, respectively. This implies that the incorporation of h-BN reduced the complex permittivity, which can be rationally interpreted by the effective medium theory [24].

### 3.3. Microwave reflection loss

The microwave absorption properties were further evaluated based on the metal back-panel model and the generalized transmission line theory [24]. The reflection loss (RL) of rGO and h-BN/rGO nano-hybrids can be obtained from the determined values of relative complex permeability and permittivity, as described by the following equations:

$$RL(dB) = 20\lg\left|\frac{\sqrt{\frac{\mu}{\varepsilon}}tanh\frac{2\pi jfd\sqrt{\varepsilon\mu}}{c} - 1}{\sqrt{\frac{\mu}{\varepsilon}}tanh\frac{2\pi jfd\sqrt{\varepsilon\mu}}{c} + 1}\right| \quad (2)$$

Where RL is the reflection loss, $d$ is the thickness of the material, $c$ is the light velocity in vacuum, $j$ is the imaginary unit, and $f$ is the frequency. The complex permeability is $\mu = \mu' - j\mu''$ and the complex permittivity is $\varepsilon' = \varepsilon' - j\varepsilon''$.

The peak frequency is generally lower with higher thickness of the material. Fig. 6 shows the reflection coefficients for rGO and BCN hybrid films, with thickness ranging from 1 to 5 mm. As shown, the microwave absorption properties of BCN50 and BCN25 hybrids were much better compared to the other samples, due to the polar group effect of h-BN/rGO nano-hybrids and the honeycomb-like structure of

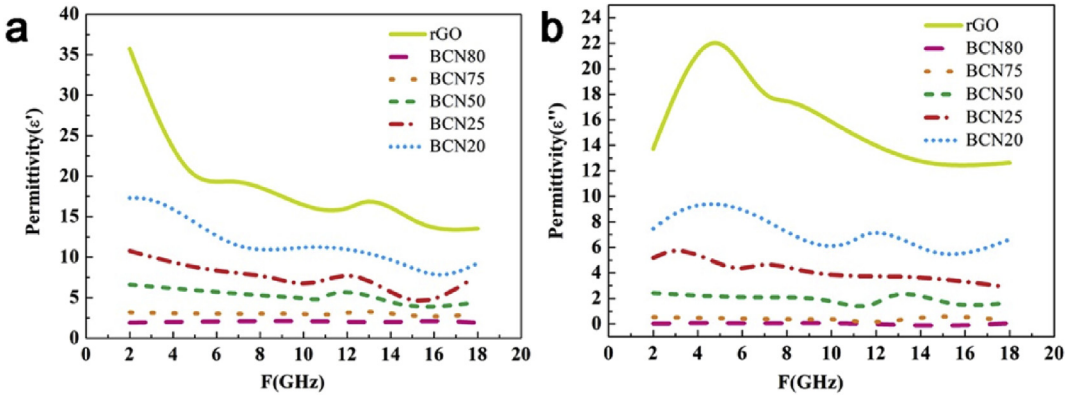


**Fig. 5.** Complex permittivity of the wax composites. (a) real part ($\varepsilon'$) and (b) imaginary part ($\varepsilon''$).

rGO. The BCN25 hybrid displayed the best microwave absorption properties. Its maximum reflection loss was −35.63 dB at 17.2 GHz and 1.8 mm, and the absorption bandwidth with reflection loss below −10 dB and −20 dB was more than 1.92 GHz (from 16.08 GHz to 18 GHz) and 0.48 GHz (from 16.96 GHz to 17.44 GHz), respectively (Table S1, Supporting Information). The effective bandwidth of BCN25 reached 6.96 GHz (from 9.28 GHz to 16.24 GHz) with 2.6 mm thickness. The maximum reflection loss of the BCN50 hybrid reached −26.07 dB at 13.6 GHz with the thickness of 2.6 mm, and the absorption bandwidth with reflection loss below −10 dB and −20 dB was more than 5.2 GHz (from 11.84 GHz to 17.04 GHz) and 1.84 GHz (from 12.8 GHz to 14.64 GHz), respectively.

As shown in Fig. 6(a), pure rGO showed some microwave absorption at 2–18 GHz due to the defect polarization relaxation, electronic dipole relaxation of the residual defects and the structure effect. However, the maximum RL was only −13.63 dB at 2.32 GHz with a thickness of 5 mm. After reacting with h-BN particles, the maximum RL of BCN20 reached −32.48 dB at 3.44 GHz with a thickness of 5 mm (Fig. 6(f)). The enhanced microwave absorption performance can be ascribed to better impedance matching. As mentioned above, rGO and BCN20 had better microwave absorbing performance when the thickness was low, and the maximum RL can be adjusted by controlling the morphologies.

### 3.4. Dielectric loss tangent

Fig. 7(a) displays the variation of the dielectric loss tangent ($\tan\delta = \frac{\varepsilon''}{\varepsilon'}$) as a function of frequency in the range of 2–18 GHz [45]. It is well known that dielectric loss tangent indicates the ability of converting microwave into other forms of energy. High dielectric loss tangent is valuable for microwave absorbing materials, while large values of $\varepsilon'$ and $\varepsilon''$ are disadvantageous for impedance matching. The ideal balance of high dielectric loss tangent and reasonable complex permittivity in BCN25 hybrid increased the RL values. In Fig. 7(a), the dielectric loss tangent increased with higher content of honeycomb-like rGO for all samples. A distinct relaxation peak appeared for rGO and BCN25 hybrid, compared to the BCN50 hybrid, due to the synchronous polarization effect and the high conductivity. The enhanced dielectric loss tangent could be ascribed to the defective porous microstructure of BCN25 hybrid, the reaction with h-BN nanosheets, and the reduction of GO, which enhanced the polarization and adjusted the conductivity. The skeleton structure provided high surface area, which was beneficial to the formation of conductive network and multi-reflection loss.

As is known, honeycomb-like rGO and h-BN/rGO nano-hybrids are dielectric loss absorbents. Debye dipolar relaxation is a significant mechanism for dielectric loss materials. The relationship between $\varepsilon'$ and $\varepsilon''$ can be expressed as follows [46]:

$$\left(\varepsilon' - \frac{\varepsilon_s + \varepsilon_\infty}{2}\right)^2 + (\varepsilon'')^2 = \left(\frac{\varepsilon_s - \varepsilon_\infty}{2}\right)^2 \quad (3)$$

$$\varepsilon' = \frac{\varepsilon''}{2\pi f\tau} + \varepsilon_\infty \quad (4)$$

Where, $\tau$, $f$, $\varepsilon_\infty$ and $\varepsilon_s$ are the polarization relaxation time, frequency, relative dielectric permittivity, and static permittivity at the high-frequency limit, respectively.

The plot of $\varepsilon'$ versus $\varepsilon''$, known as the Cole-Cole semicircle, is a single semicircle corresponding to one Debye relaxation [47–49]. The semicircles are related to the interfacial relaxation and Debye dipolar relaxation, which are usually induced by a delay in molecular polarization with regard to dynamic electric fields in a dielectric medium.

The Cole-Cole plots in Fig. 7(b–d) illustrate the response behavior of the hybrids in the frequency range of 2–18 GHz. For the BCN25 hybrid, three Cole-Cole semicircles were observed in Fig. 7(c), implying that the relaxations resulted from multiple mechanisms of interface polarization and electron polarization. The phenomenon was credited to the presence of more heterogeneous interfaces between rGO and h-BN nanosheets, which increased the number of large dipoles and the interfacial polarization. Other kinds of relaxation may also occur in these hybrids, such as Maxwell-Wagner-Sillars relaxation, defect polarization, electron polarization, etc. For rGO, two small Cole-Cole semicircles were observed in Fig. 7(b). The comparison of Fig. 7(b) and (c) indicates that the incorporation of h-BN with rGO introduced relaxation processes, which significantly improved the microwave absorption properties of h-BN-rGO hybrids. Similarly, with increase in h-BN content in the composites, decreased semicircles were observed for the BCN50 hybrid (Fig. 7(d)). This result indicated that chemical bonds, defects, or interfaces in BCN50 hybrid contributed little to the dielectric loss. The polarization relaxation process was overshadowed by the carrier mobility.

### 3.5. Impedance matching performance

The characteristic impedance can be used to evaluate the impedance matching performance of materials. The characteristic impedance of

**Table 4**
Electrical properties of rGO and h-BN/rGO nano-hybrids.

| Sample | rGO | BCN20 | BCN25 | BCN50 | BCN75 | BCN80 |
|---|---|---|---|---|---|---|
| Resistance/(Ω) | $6.66 \times 10^{-3}$ | $75.5 \times 10^{-3}$ | $83.9 \times 10^{-3}$ | 0.68 | 3.9 | $4.3 \times 10^{3}$ |

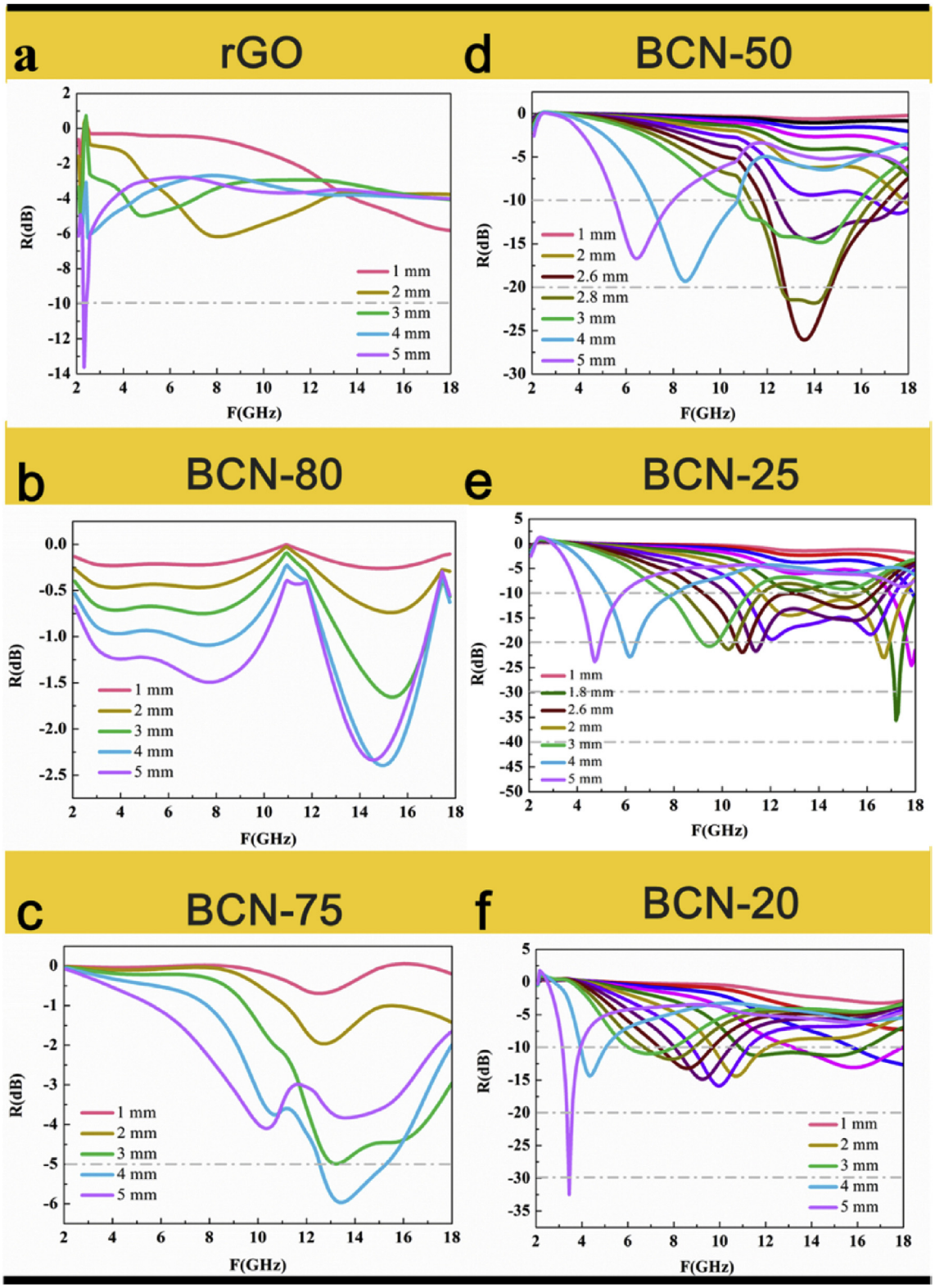


**Fig. 6.** Frequency dependence of the reflection coefficient on the thickness of the paraffin composites of (a) rGO, (b) BCN80, (c) BCN75, (d) BCN50, (e) BCN25, (f) BCN20.

materials should be as close to the impedance of free air as possible. The characteristic impedance ($Z_{im}$) is expressed by the relative complex permittivity and permeability [50,51]:

$$Z_{im} = \sqrt{\frac{\mu_0}{\varepsilon_0}}\sqrt{\frac{\mu_r}{\varepsilon_r}} \quad (5)$$

The characteristic impedance of rGO ranged from 0.16 to 0.45, which was much lower than that of air (Z = 1). The characteristic impedance values for BCN20, BCN25, and BCN50 were substantially improved compared to rGO and were closer to the impedance of air (see Fig. 8). According to the impedance matching theory [50,51], the reflection of EM waves on the surfaces of BCN20, BCN25, and BCN50 will

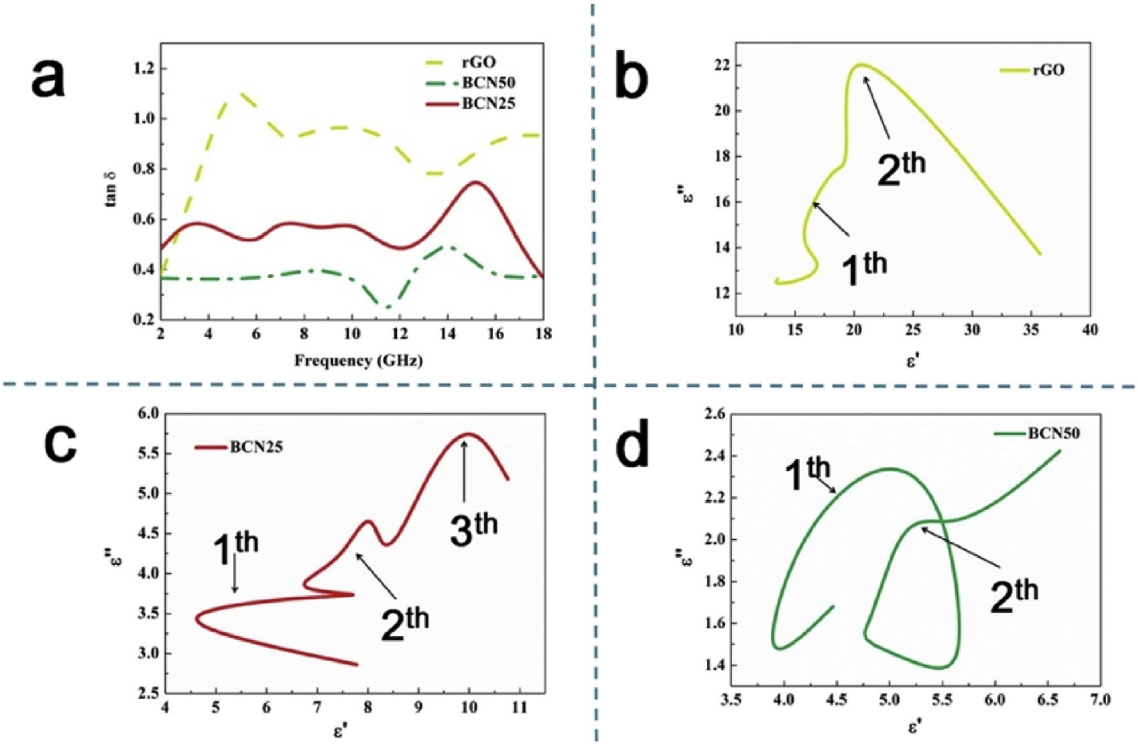


**Fig. 7.** (a) Loss tangents of the wax composites; (c–d) ε′-ε′′ curves of the rGO and h-BN/rGO nano-hybrids.

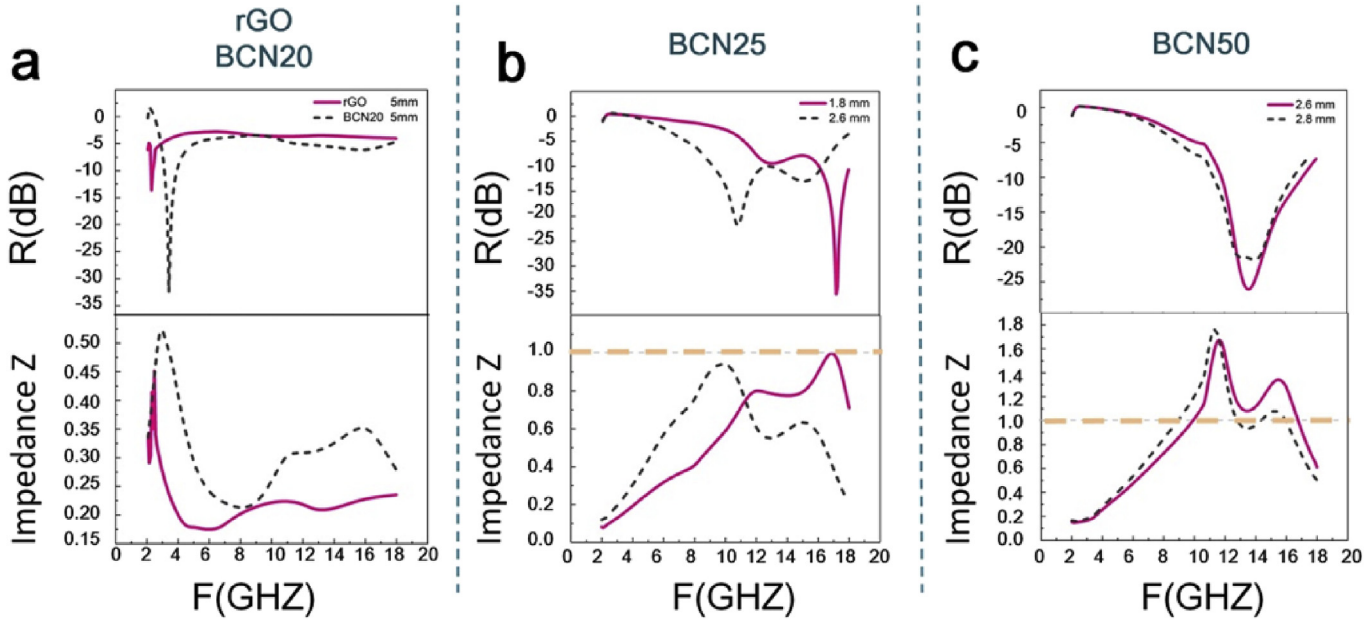


**Fig. 8.** (a–c) Characteristic impedance versus frequency for sample of rGO, BCN50, BCN25, and BCN20.

decrease, compared with rGO. Thus, most of the EM waves can enter the absorbing materials and be dissipated. This result is consistent with the expectations from our original material design. Based on the above discussion, impedance matching is mainly responsible for improved EM-wave absorption properties. Thus, the introduction of h-BN nanolayers was helpful in improving the properties of the resulting BCN20, BCN25, and BCN50 hybrids.

To better evaluate the EM absorption performance of the materials in this study, the EM wave absorbing properties of similar materials reported in literature, including GFs and typical carbon-based composites, are summarized and compared in Fig. 9(a) and Table S2 [18,24,52–55].

The minimum value of RL for GF is reported to be about −30 dB [18]. However, in the present work, h-BN/rGO nano-hybrids with the distinct structures composed of rGO substrate demonstrated much stronger EM absorption properties than previously reported materials. Compared with former composites, the honeycomb architecture of h-BN/rGO nano-hybrids displayed lower bulk density, strong absorption intensity, wide effective absorption bandwidth and small thickness. Moreover, the minimum RL value of h-BN/rGO nano-hybrids was as low as −35.63 dB, and the absorption bandwidth with reflection loss below −10 dB was more than 6.96 GHz, indicating that these are

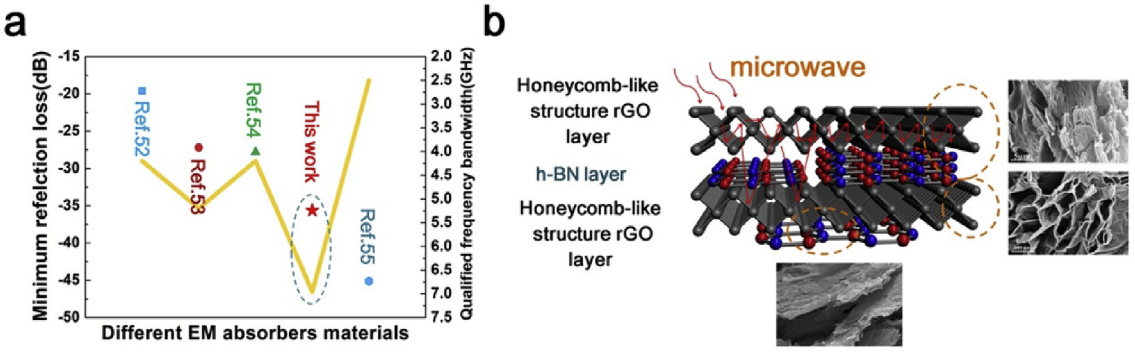


**Fig. 9.** (a) Comparison of minimum reflection losses and effective absorption bandwidth of different EM absorbers reported in the literature. (b) Illustration of the microwave consumption.

excellent EM absorbing materials.

Fig. 9(b) presents the proposed mechanism of the microwave absorption of h-BN/rGO nano-hybrids [56,57]. Firstly, the individual 3D interconnected graphene network of h-BN/rGO nano-hybrids played a key role in the substantially enhanced microwave absorption behavior [18]. The intricate reticulated structures consisting of entangled conductive graphene sheets spontaneously responded to the incident microwave as currents induced by resistance–inductance–capacitance coupled circuits and time-varying electromagnetic fields occurred on cell walls and struts of the h-BN/rGO nano-hybrids. Such long-range induced currents quickly attenuated in the resistive network and converted into thermal energy, leading to rapid decay of the incident electromagnetic wave. Moreover, as stated in our previous work [24], the microwaves multiplied into the wax composites containing the h-BN/rGO nano-hybrids, resulting in free electrons in the honeycomb-like rGO framework. The newly generated electrons in the honeycomb-like rGO framework migrated freely in the hybrids, hopped across the interfaces between the graphene layers, and had a greater influence on the increase in value of $\varepsilon''$ than that of $\varepsilon'$. Moreover, the incorporation of immobilized h-BN into the honeycomb-like rGO created grain boundaries, which contributed to the formation of capacitor-like structure and polarization at the interfaces. Therefore, h-BN had a larger influence on the increase in value of $\varepsilon'$ than that of $\varepsilon''$.

## 4. Conclusions

Under a fast and simple microwave treatment, GO and h-BN stacked into GO-h-BN assemblies and transformed into honeycomb architecture of h-BN/rGO nano-hybrids. The content of h-BN was controlled by changing the mass ratio of raw materials. When the mass ratio of GO/h-BN was 2:1, the microwave absorbing capacity of the BCN25 hybrid was excellent in the range of 9–18 GHz. The minimum RL of the wax composite filled with 6.25 wt% BCN25 with thickness of 1.8 mm was −35.63 dB at 17.2 GHz. At this low thickness, the frequency bandwidth (RL ≤ −10 dB) of 1.92 GHz was achieved. The high dielectric loss tangent and the good impedance matching resulted from graphene-based conductivity and h-BN-related defects, respectively. The honeycomb-like structure provided a large number of reflecting channels for microwave consumption. The lightweight hybrids were easily obtained on a large scale with low cost. Hence, these materials show promise for applications in both military and civil fields.

## Acknowledgements

The project was financially supported by National Natural Science Foundation of China (No. 11404397 and No.51602283).

## Appendix A. Supplementary data

Supplementary data to this article can be found online at https://doi.org/10.1016/j.compscitech.2019.02.029.

## References

[1] L. Wang, Y. Huang, C. Li, J.J. Chen, X. Sun, A facile one-pot method to synthesize a three-dimensional graphene@carbon nanotube composite as a high-efficiency microwave absorber, Phys. Chem. Chem. Phys. 17 (3) (2015) 2228–2234.
[2] W.C. Li, C. Le, J.J. Lv, W. Huang, L. Qiao, J.W. Zheng, et al., Electromagnetic and oxidation resistance properties of core-shell structure flaked carbonyl iron powder@SiO2 nanocomposite, Phys. Status Solidi Appl. Mater. Sci. 214 (6) (2017).
[3] Y.H. Cheng, P. Hu, S.B. Zhou, L.W. Yan, B.Q. Sun, X.H. Zhang, et al., Achieving tunability of effective electromagnetic wave absorption between the whole X-band and Ku-band via adjusting PPy loading in SiC nanowires/graphene hybrid foam, Carbon 132 (2018) 430–443.
[4] W. Li, Q. Liu, L. Wang, Z. Zhou, J. Zheng, Y. Ying, et al., Low frequency and broadband metamaterial absorber with cross arrays and a flaked iron powder magnetic composite, AIP Adv. 8 (1) (2018).
[5] W. Li, X. Zhou, Y. Ying, X. Qiao, F. Qin, Q. Li, et al., Polarization-insensitive wide-angle multiband metamaterial absorber with a double-layer modified electric ring resonator array, AIP Adv. 5 (6) (2015) 067151.
[6] L. Wei, Q. Shao, G. Ji, X. Liang, C. Yan, B. Quan, et al., Metal – organic-frameworks derived porous carbon-wrapped Ni composites with optimized impedance matching as excellent lightweight electromagnetic wave absorber, Chem. Eng. J. 313 (2017) 734–744.
[7] C. Yan, Z. Li, L. Yong, S. Dai, G. Ji, H. Zhao, et al., Rationally regulating complex dielectric parameters of mesoporous carbon hollow spheres to carry out efficient microwave absorption, Carbon 127 (2018) 643–652.
[8] H. Lv, Z. Yang, P.L. Wang, G. Ji, J. Song, L. Zheng, et al., A voltage-boosting strategy enabling a low-frequency, flexible electromagnetic wave absorption device, Adv. Mater. 30 (15) (2018) 1706343.
[9] J. Ma, J. Shu, W. Cao, M. Zhang, X. Wang, J. Yuan, et al., A green fabrication and variable temperature electromagnetic properties for thermal stable microwave absorption towards flower-like Co3O4@rGO/SiO2 composites, Compos. B Eng. 166 (2019) 187–195.
[10] B. Wen, M.S. Cao, M.M. Lu, W.Q. Cao, H.L. Shi, J. Liu, et al., Reduced graphene oxides: light-weight and high-efficiency electromagnetic interference shielding at elevated temperatures, Adv. Mater. 26 (21) (2014) 3484–3489.
[11] B. Quan, X.H. Lang, G.B. Ji, J.N. Ma, P.Y. Ouyang, H. Gong, et al., Strong electromagnetic wave response derived from the construction of dielectric/magnetic media heterostructure and multiple interfaces, ACS Appl. Mater. Interfaces 9 (11) (2017) 9964–9974.
[12] W. Liu, L. Liu, Z.H. Yang, J.J. Xu, Y.L. Hou, G.B. Ji, A versatile route toward the electromagnetic functionalization of metal-organic framework-derived three-dimensional nanoporous carbon composites, ACS Appl. Mater. Interfaces 10 (10) (2018) 8965–8975.
[13] X.M. Zhang, G.B. Ji, W. Liu, X.X. Zhang, Q.W. Gao, Y.C. Li, et al., A novel Co/TiO2 nanocomposite derived from a metal-organic framework: synthesis and efficient microwave absorption, J. Mater. Chem. C 4 (9) (2016) 1860–1870.
[14] M.S. Cao, Y.Z. Cai, P. He, J.C. Shu, W.Q. Cao, J. Yuan, 2D MXenes: electromagnetic property for microwave absorption and electromagnetic interference shielding, Chem. Eng. J. 359 (2019) 1265–1302.
[15] H.J. Yang, M.S. Cao, Y. Li, H.L. Shi, Z.L. Hou, X.Y. Fang, et al., Enhanced dielectric properties and excellent microwave absorption of SiC powders driven with NiO nanorings, Adv. Opt. Mater. 2 (3) (2014) 214–219.
[16] Y. Liu, Y.C. Zhang, X. Wang, Z.M. Wang, W.C. Lai, X.J. Zhang, et al., Excellent microwave absorbing property of multiwalled carbon nanotubes with skin-core heterostructure formed by outer dominated fluorination, J. Phys. Chem. C 122 (11) (2018) 6357–6367.
[17] C. Chen, J.B. Xi, E.Z. Zhou, L. Peng, Z.C. Chen, C. Gao, Porous graphene

microflowers for high-performance microwave absorption, Nano-Micro Lett. 10 (2) (2018).
[18] Y. Zhang, Y. Huang, T.F. Zhang, H.C. Chang, P.S. Xiao, H.H. Chen, et al., Broadband and tunable high-performance microwave absorption of an ultralight and highly compressible graphene foam, Adv. Mater. 27 (12) (2015) 2049–2053.
[19] C. Wang, X.J. Han, P. Xu, X.L. Zhang, Y.C. Du, S.R. Hu, et al., The electromagnetic property of chemically reduced graphene oxide and its application as microwave absorbing material, Appl. Phys. Lett. 98 (7) (2011).
[20] X.C. Dong, Y.M. Shi, Y. Zhao, D.M. Chen, J. Ye, Y.G. Yao, et al., Symmetry breaking of graphene monolayers by molecular decoration, Phys. Rev. Lett. 102 (13) (2009).
[21] H. Huang, S. Chen, X.Y. Gao, W. Chen, A.T.S. Wee, Structural and electronic properties of PTCDA thin films on epitaxial graphene, ACS Nano 3 (11) (2009) 3431–3436.
[22] X. Deng, M.S. Si, J.Y. Dai, Communication: oscillated band gaps of B/N-codoped alpha-graphyne, J. Chem. Phys. 137 (20) (2012).
[23] Y. Kang, Z.Y. Chu, D.J. Zhang, G.Y. Li, Z.H. Jiang, H.F. Cheng, et al., Incorporate boron and nitrogen into graphene to make BCN hybrid nanosheets with enhanced microwave absorbing properties, Carbon 61 (2013) 200–208.
[24] Y. Kang, Z.H. Jiang, T. Ma, Z.Y. Chu, G.Y. Li, Hybrids of reduced graphene oxide and hexagonal boron nitride: lightweight Absorbers with tunable and highly efficient microwave attenuation properties, ACS Appl. Mater. Interfaces 8 (47) (2016) 32468–32476.
[25] L. Song, Z. Liu, A.L.M. Reddy, N.T. Narayanan, J. Taha-Tijerina, J. Peng, et al., Binary and ternary atomic layers built from carbon, boron, and nitrogen, Adv. Mater. 24 (36) (2012) 4878–4895.
[26] L. Ci, L. Song, C.H. Jin, D. Jariwala, D.X. Wu, Y.J. Li, et al., Atomic layers of hybridized boron nitride and graphene domains, Nat. Mater. 9 (5) (2010) 430–435.
[27] H.J. Yin, S.L. Zhao, J.W. Wan, H.J. Tang, L. Chang, L.C. He, et al., Three-dimensional graphene/metal oxide nanoparticle hybrids for high-performance capacitive deionization of saline water, Adv. Mater. 25 (43) (2013) 6270–6276.
[28] H. Hu, Z.B. Zhao, Q. Zhou, Y. Gogotsi, J.S. Qiu, The role of microwave absorption on formation of graphene from graphite oxide, Carbon 50 (9) (2012) 3267–3273.
[29] D. Voiry, J. Yang, J. Kupferberg, R. Fullon, C. Lee, H.Y. Jeong, et al., High-quality graphene via microwave reduction of solution-exfoliated graphene oxide, Science 353 (6306) (2016) 1413–1416.
[30] I.T. Kim, M.J. Song, Y.B. Kim, M.W. Shin, Microwave-hydrothermal synthesis of boron/nitrogen co-doped graphene as an efficient metal-free electrocatalyst for oxygen reduction reaction, Int. J. Hydrogen Energy 41 (47) (2016) 22026–22033.
[31] G. Lian, X. Zhang, M. Tan, S.J. Zhang, D.L. Cui, Q.L. Wang, Facile synthesis of 3D boron nitride nanoflowers composed of vertically aligned nanoflakes and fabrication of graphene-like BN by exfoliation, J. Mater. Chem. 21 (25) (2011) 9201–9207.
[32] Z.W. Tang, H. Chen, X.W. Chen, L.M. Wu, X.B. Yu, Graphene oxide based recyclable dehydrogenation of ammonia borane within a hybrid nanostructure, J. Am. Chem. Soc. 134 (12) (2012) 5464–5467.
[33] D.C. Wei, Y.Q. Liu, Y. Wang, H.L. Zhang, L.P. Huang, G. Yu, Synthesis of N-doped graphene by chemical vapor deposition and its electrical properties, Nano Lett. 9 (5) (2009) 1752–1758.
[34] T. Zhang, J. Zhang, H. Luo, L.W. Deng, P.Y. Zhou, G.W. Wen, et al., Facile approach to fabricate BCN/Fe-x(B/C/N)(y) nano-architectures with enhanced electromagnetic wave absorption, Nanotechnology 29 (23) (2018).
[35] A. Nag, K. Raidongia, K. Hembram, R. Datta, U.V. Waghmare, C.N.R. Rao, Graphene analogues of BN: novel synthesis and properties, ACS Nano 4 (3) (2010) 1539–1544.
[36] L.G. Cancado, A. Jorio, E.H.M. Ferreira, F. Stavale, C.A. Achete, R.B. Capaz, et al., Quantifying defects in graphene via Raman spectroscopy at different excitation energies, Nano Lett. 11 (8) (2011) 3190–3196.
[37] B. Li, L. Zhou, D. Wu, H.L. Peng, K. Yan, Y. Zhou, et al., Photochemical chlorination of graphene, ACS Nano 5 (7) (2011) 5957–5961.
[38] S. Dou, X.B. Huang, Z.L. Ma, J.H. Wu, S.Y. Wang, A simple approach to the synthesis of BCN graphene with high capacitance, Nanotechnology 26 (4) (2015).
[39] Z.J. Fan, W. Kai, J. Yan, T. Wei, L.J. Zhi, J. Feng, et al., Facile synthesis of graphene nanosheets via Fe reduction of exfoliated graphite oxide, ACS Nano 5 (1) (2011) 191–198.
[40] M. Hubáček, T. Sato, T. Ishii, A coexistence of boron nitride and boric oxide, J. Solid State Chem. 109 (2) (1994) 384–390.
[41] V. Brožek, M. Hubáček, A contribution to the crystallochemistry of boron nitride, J. Solid State Chem. 100 (1) (1992) 120–129.
[42] T.W. Lin, C.Y. Su, X.Q. Zhang, W.J. Zhang, Y.H. Lee, C.W. Chu, et al., Converting graphene oxide monolayers into boron carbonitride nanosheets by substitutional doping, Small 8 (9) (2012) 1384–1391.
[43] K. Raidongia, A. Nag, K. Hembram, U.V. Waghmare, R. Datta, C.N.R. Rao, BCN: a graphene analogue with remarkable adsorptive properties, Chem. Eur. J. 16 (1) (2010) 149–157.
[44] K. Zhang, X. Gao, Q. Zhang, X. Chen, Carbon coated paramagnetic Fe3O4 nanoparticles decorated MWCNTs-GNS composites: synthesis, characterization and their excellent electromagnetic absorption properties, J. Mater. Sci. Mater. Electron. 29 (4) (2018) 3401–3410.
[45] J. Tauc, R. Grigorovici, A. Vancu, Optical properties and electronic structure of amorphous germanium, Phys. Status Solidi (b) 15 (2) (1966) 627–637.
[46] B. Zhao, G. Shao, B.B. Fan, W.Y. Zhao, Y.J. Xie, R. Zhang, Synthesis of flower-like CuS hollow microspheres based on nanoflakes self-assembly and their microwave absorption properties, J. Mater. Chem. A 3 (19) (2015) 10345–10352.
[47] S. Qiu, H.L. Lyu, J.R. Liu, Y.Z. Liu, N.N. Wu, W. Liu, Facile synthesis of porous nickel/carbon composite microspheres with enhanced electromagnetic wave absorption by magnetic and dielectric losses, ACS Appl. Mater. Interfaces 8 (31) (2016) 20258–20266.
[48] B.A. Zhao, G. Shao, B.B. Fan, W.Y. Zhao, R. Zhang, Facile synthesis and enhanced microwave absorption properties of novel hierarchical heterostructures based on a Ni microsphere-CuO nano-rice core-shell composite, Phys. Chem. Chem. Phys. 17 (8) (2015) 6044–6052.
[49] X. Jian, B.A. Wu, Y.F. Wei, S.X. Dou, X.L. Wang, W.D. He, et al., Facile synthesis of Fe3O4/GCs composites and their enhanced microwave absorption properties, ACS Appl. Mater. Interfaces 8 (9) (2016) 6101–6109.
[50] M.S. Cao, W.L. Song, Z.L. Hou, B. Wen, J. Yuan, The effects of temperature and frequency on the dielectric properties, electromagnetic interference shielding and microwave-absorption of short carbon fiber/silica composites, Carbon 48 (3) (2010) 788–796.
[51] X. Wang, J.C. Shu, X.M. He, M. Zhang, X.X. Wang, C. Gao, et al., Green approach to conductive PEDOT:PSS decorating magnetic-graphene to recover conductivity for highly efficient absorption, ACS Sustain. Chem. Eng. 6 (11) (2018) 14017–14025.
[52] M.K. Han, X.W. Yin, Z.X. Hou, C.Q. Song, X.L. Li, L.T. Zhang, et al., Flexible and thermostable graphene/SiC nanowire foam composites with tunable electromagnetic wave absorption properties, ACS Appl. Mater. Interfaces 9 (13) (2017) 11803–11810.
[53] J.N. Ma, W. Liu, B. Quan, X.H. Liang, G.B. Ji, Incorporation of the polarization point on the graphene aerogel to achieve strong dielectric loss behavior, J. Colloid Interface Sci. 504 (2017) 479–484.
[54] C.Q. Song, X.W. Yin, M.K. Han, X.L. Li, Z.X. Hou, L.T. Zhang, et al., Three-dimensional reduced graphene oxide foam modified with ZnO nanowires for enhanced microwave absorption properties, Carbon 116 (2017) 50–58.
[55] C.H. Wang, Y.J. Ding, Y. Yuan, X.D. He, S.T. Wu, S. Hu, et al., Graphene aerogel composites derived from recycled cigarette filters for electromagnetic wave absorption, J. Mater. Chem. C 3 (45) (2015) 11893–11901.
[56] M.S. Cao, X.X. Wang, W.Q. Cao, X.Y. Fang, B. Wen, J. Yuan, Thermally driven transport and relaxation switching self-powered electromagnetic energy conversion, Small 14 (29) (2018).
[57] W.Q. Cao, X.X. Wang, J. Yuan, W.Z. Wang, M.S. Cao, Temperature dependent microwave absorption of ultrathin graphene composites, J. Mater. Chem. C 3 (38) (2015) 10017–10022.